

Paper-based genetic assays with bioconjugated gold nanorods and an automated readout pipeline

Claudia Borri

Consiglio Nazionale delle Ricerche

Sonia Centi (✉ s.centi@ifac.cnr.it)

National Council of Italy <https://orcid.org/0000-0001-5432-5589>

Sofia Chioccioli

Università degli Studi di Firenze: Università degli Studi di Firenze

Patrizia Bogani

Università degli Studi di Firenze

Filippo Micheletti

Consiglio Nazionale delle Ricerche

Marco Gai

Consiglio Nazionale delle Ricerche

Paolo Grandi

Laboratori Victoria s.r.l.

Serena Laschi

Ecobioservices & Researches s.r.l.

Francesco Tona

Ecobioservices & Researches s.r.l.

Andrea Barucci

Consiglio Nazionale delle Ricerche

Nicola Zoppetti

Consiglio Nazionale delle Ricerche

Roberto Pini

Consiglio Nazionale delle Ricerche

Fulvio Ratto

Consiglio Nazionale delle Ricerche

Research Article

Keywords: Gold nanorods, rolC gene, PCR, dot-blot assays, standardized photography, image regression

Posted Date: October 20th, 2021

DOI: <https://doi.org/10.21203/rs.3.rs-978292/v1>

License:  This work is licensed under a Creative Commons Attribution 4.0 International License.

[Read Full License](#)

Version of Record: A version of this preprint was published at Scientific Reports on April 13th, 2022. See the published version at <https://doi.org/10.1038/s41598-022-10227-7>.

Paper-based genetic assays with bioconjugated gold nanorods and an automated readout pipeline

Claudia Borri, Sonia Centi*, Sofia Chioccioli, Patrizia Bogani, Filippo Micheletti, Marco Gai, Paolo Grandi, Serena Laschi, Francesco Tona, Andrea Barucci, Nicola Zoppetti, Roberto Pini, Fulvio Ratto

*Corresponding author: s.centi@ifac.cnr.it

Abstract

Background: Paper-based biosensors featuring immunoconjugated gold nanoparticles have gained extraordinary momentum in recent times as the platform of choice in key cases of field applications, including the so-called rapid antigen tests for SARS-CoV-2. Here, we propose a revision of this format, one that may leverage on the most recent advances in materials science and data processing. In particular, we focus on an amplifiable DNA rather than a protein target, and we assess the replacement of gold nanospheres with anisotropic nanorods, which are about 10-fold brighter and multiplexable. **Results:** By comparison with a gold-standard method for dot-blot readout with digoxigenin, we show that gold nanorods entail much faster and easier processing, at the cost of a higher detection limit (from below 1 to 10 ppm in the case of plasmid DNA containing a target transgene). In addition, we test a complete workflow for systematic acquisition and machine-learning regression of photographs of dot-blot membranes as a tool to gain more analytical sensitivity and potential for quantification. A leave-one-out strategy for training and validation with as few as 36 sample instances already improves the detection limit reached by the naked eye by a factor around 2. **Conclusions:** Taken together, we conjecture that the synergistic combination of new materials and innovative tools for data processing may bring the analytical sensitivity of paper-based biosensors to approach the level of lab-grade molecular tests.

Keywords

Gold nanorods; rolC gene; PCR; dot-blot assays; standardized photography; image regression

Background

In the last twenty years, plasmonic nanoparticles have sparked more and more interest for their chemical and optical versatility, biocompatibility, stability and efficiency as optical labels or contrast

agents for biosensing, biomedical imaging, Raman or luminescence spectroscopy, controlled release and delivery of drugs, the optical hyperthermia of cancer and many other applications [1–5].

In particular, thanks to their photophysical properties and ease of chemical synthesis, gold nanoparticles (AuNPs) stand out as an excellent choice to develop a plethora of colorimetric biosensors. Colloidal suspensions of AuNPs display different colors depending on their size, shape, state of aggregation and environment [3, 6, 7]. It is relatively simple to modify their surface with functional biomolecules like proteins [8, 9], such as antibodies [10, 11] and enzymes [12, 13], aptamers [14, 15], other oligonucleotides [16, 17], or polysaccharides [18–20]. Relevant methods include protocols for both passive absorption (i.e. van der Waals, ionic or hydrophobic interactions) and the formation of covalent bonds (e.g. amidation and thiolation). The bioconjugation of AuNPs has reached such a level of refinement that it is possible to tune parameters like, for instance, the orientation of antibodies sitting on their surface [9, 21].

The bright colors of AuNPs originate from localized surface plasmon resonance (LSPR) oscillations, and so exhibit sensitivity to any variation of their near-field landscape. By assessing the accumulation, aggregation or modification of AuNPs, it is indeed possible to visualize specific biomolecular interactions in suspension or on paper-based supports [22–24]. The LSPR phenomenon has been exploited in e.g. colloidal nanoparticle-based ELISA sensors [25], colorimetric immunoassays [26, 27], standard lateral flow assays [28, 29], and many more inventive methods. For instance, the aggregation of AuNPs has been used as a mechanism to modulate the enhancement of Raman signals [30]. The particular case of paper-based biosensors with immunoconjugated AuNPs has played an extraordinary role in the recent COVID-19 outbreak, as the technological platform implemented in the so-called rapid antigen-tests. However, in spite of their incredible success, these systems have also revealed weaknesses: their analytical sensitivity amounts to several hundred units of Median Tissue Culture Infectious Dose (TCID₅₀) per ml [31, 32], which is at least two to three orders of magnitude worse than that of Polymerase Chain Reaction (PCR)-based tests [33], and their large-scale use is qualitative only.

Here, we describe a synergistic set of solutions that collectively aim at a more sensitive and quantitative use of paper-based biosensors with bioconjugated AuNPs. First, we focus on DNA rather than a protein target. Second, we test the use of anisotropic AuNPs, such as gold nanorods (AuNRs). And third, we assess the feasibility of machine learning for a scenario of automatic readout. In order to keep control over all kinetic parameters, we implement a dot-blot setup as a convenient model of a paper-based assay.

The use of DNA targets in lateral flow assays provides the unique advantage of compatibility with PCR-based [34–36] or isothermal [37–39] protocols of amplification. The detection of genetic markers is a

fundamental tool in various contexts, such as medical diagnostics, forensics, agriculture and environmental monitoring. In particular, the identification of pathogenetic targets is a frontier of extreme interest in clinical and environmental fields, e.g. to profile the microorganisms involved in infections and to trace the diffusion of antibiotic resistance or genetically modified organisms. In this work, we chose the *rolC* gene as a well-known model, which is an ideal candidate for plant genetic engineering [40]. The *Agrobacterium rhizogenes rol* oncogenes regulate plant growth, cell differentiation and secondary metabolism in transformed cells from several plant families [41]. It has also been suggested that the expression of these genes may have played a key role in evolution [42, 43] and in the establishment of new species [44].

By coming in multiple and much brighter colors, AuNRs outperform their isotropic predecessors in several respects. The efficiency of optical absorbance of AuNRs is about 10 times larger than that of spherical AuNPs [6, 45, 46], which translates into a better visibility and so presumably an earlier detectability in colorimetric setups. In addition, the color of AuNRs depends on their aspect ratio (AR = length / diameter), which is an easy parameter to tune in their synthesis, and so a degree of freedom available for multiplexing. The fabrication of AuNRs displaying AR greater than around 4 and resonating at deep-penetrating near-infrared frequencies is a recurrent solution in nanomedicine for applications like the optical hyperthermia and photoacoustic imaging of cancer [47–51]. However, when it comes to their functionalization with nucleotide probes, the switch from spherical AuNPs to AuNRs is nontrivial, because their surface-chemistry is different and, in particular, the electrokinetic potential of their as-synthesized colloids usually flips from anionic to strongly cationic. The modification of AuNRs with citrate [52, 53] has become a strategic niche of colloidal chemistry to emulate the surface-chemistry of spherical AuNPs, and so enable a smooth transfer of a plethora of protocols developed in decades of relevant experience.

The application of artificial intelligence to the interpretation of dot-blot assays is a cutting-edge idea that may help fulfill their quantitative readout. The coloration pattern within each blot is often irregular and non-uniform, which complicates a traditional analysis of measurable signals like the intensity of diffuse optical reflectance [9] or surface enhance Raman scattering [54, 55], in the case of active tags. As a consequence, the typical use of these predictors is qualitative only or semi-quantitative, at best. Here, we assess the feasibility of a supervised machine learning approach to the regression of standardized photographs of dot-blot assays as a tool to go far beyond their qualitative readout. The application of artificial intelligence to the objective interpretation of biomedical images of all sorts, including e.g. micrographs, tomographs or endoscopies of cells [56], tissues [57, 58] or patients [59, 60], is becoming a mainstream paradigm to identify hidden patterns and support clinical decisions at any level. In the context of paper-based assays, for instance, A. Carrio et al developed a light box and a pipeline based on a multilayer perceptron artificial neural network for the classification of results from commercial lateral flow tests

for the detection of drugs of abuse in the saliva [61]. Other authors used linear support vector machines to classify images of lateral flow strips [62, 63] or pH indicator papers [64]. However, the step from classification between discrete bins to regression against a continuous scale is another key challenge on the path of analytical quantification.

Here, we propose a systems engineering perspective on the refinement of paper-based assays, where we pursue a holistic redesign of all components from materials to hardware and software, in order to leverage on new synergies between topical developments made in complementary subfields of science and technology.

Methods

Materials

Cetrimonium bromide (CTAB), tri-sodium citrate dihydrate, poly(sodium 4-styrenesulfonate), Tween® 20, Tris(2-carboxyethyl)phosphine hydrochloride, sodium chloride, sodium dodecyl sulfate, agarose, Tris-Borate EDTA buffer, and all chemicals for the synthesis of AuNRs were purchased from MilliporeSigma (Merck KGaA, Germany). Dulbecco's Phosphate-Buffered Saline (DPBS) was supplied by PAN™-Biotech (Germany). Unmodified PCR primers and all complementary target sequences were obtained from Eurofins Genomics (Eurofins Scientific, Germany) and dNTPs from BioChain® (BioChain Institute, USA).

Preparation of gold nanorods

Cetrimonium-coated AuNRs were synthesized according to the prescriptions reported by X. Ye et al [65], and in particular the case featuring 47 mM CTAB, 8.3 mM sodium oleate, 180 μ M AgNO₃, 3.4 mM HCl and 0.038% seed solution, which conveys an average AR around 3.9.

In order to obtain an anionic electrokinetic potential, CTAB was gradually replaced with tri-sodium citrate dihydrate (Na₃-citrate), by following and modifying the procedure reported by J. G. Mehtala et al [52]. In our modification, AuNRs were initially incubated with an aqueous solution of 0.15% poly(sodium 4-styrenesulfonate) (Na-PSS), also containing 0.5 mM CTAB, which confers more colloidal stability in this critical passage, for 24 hours at RT under gentle stirring. After three cycles of centrifugation at 11.000 g and resuspension in 0.15% Na-PSS, AuNRs were transferred into an aqueous solution of 5 mM Na₃-citrate, left at rest for further 24 hours, purified by two cycles of centrifugation, and finally stored at a nominal concentration of 1.6 mM Au in 5 mM Na₃-citrate, until use.

Citrate-stabilized AuNRs were characterized by dynamic light scattering (DLS) (NANO-ZS90 Zetasizer, Malvern Instruments, UK), UV-visible spectrophotometry (BioSpectrometer® basic, Eppendorf, Germany) and gel electrophoresis (PerfectBlue™ Horizontal Mini Gel System, PEQLAB Biotechnologie, Germany).

Preparation of DNA molecular probes

Two different nucleotide probes were chosen for bio-conjugation of the AuNRs (Table 1).

The first one consisted of a synthetic 21-mer DNA oligonucleotide, which was modified with a tail of 20 thymine bases and a terminal thiol at its 5'-end (Metabion International AG, Germany). This short sequence was also used as specific forward primer for *rolC* gene in an end-point PCR process (T100™ Thermal Cycler, Bio-Rad Laboratories, USA).

The second probe was a 328-mer single-stranded DNA sequence, which was derived by a 328-bp double-stranded *rolC* amplified fragment. The template for PCR amplification was the pUC19 cloning vector (New England Biolabs, USA), containing a 1860-bp *Agrobacterium rhizogenes* (strain 1855) HindIII-EcoRI restriction fragment that encompassed both the promoter and the coding region of *rolC* gene (ORF12) [66]. The HindIII-EcoRI fragment was cloned into the pUC19 polylinker restriction sites and ligated with T4 DNA ligase (New England Biolabs, USA). About 1 ng of this template was amplified by end-point PCR with the specific thiol-labeled forward and an unmodified reverse primer at an annealing temperature of 55°C, in several replicates. In this manner, amplicon molecules were generated with terminal thiols at the 5'-ends of their sense strands. A typical PCR reaction mixture contained 200 nM of each primer (Table 1), 800 μM dNTPs and 0.05 U/μl DreamTaq™ DNA Polymerase (Thermo Scientific™, Thermo Fisher Scientific, USA). At the end of 35 cycles, each product was purified by MicroSpin™ columns (illustra™ GFX™ PCR DNA and gel band purification kit, GE Healthcare, UK), according to the instructions provided by the manufacturer and by eluting with 10 mM Tris-HCl buffer (pH 8.0). The concentration of the purified amplicon was finally quantified by a Qubit™ fluorometer (Invitrogen™, Thermo Fisher Scientific, USA).

Functionalization of gold nanorods with DNA molecular probes

The stock suspension of citrate-stabilized AuNRs was transferred into a 0.5 mM Na₃-citrate solution containing 0.005% Tween® 20, at the nominal concentration of 0.8 mM Au.

In the meantime, both thiolated nucleotide probes were treated with 10 mM Tris(2-carboxyethyl)phosphine hydrochloride) (TCEP) for 1 hour at RT, in order to reduce potential disulfide bridges into more reactive thiols. A thermal denaturation step was required for the *rolC* amplicon to split into single strands.

About 4 μM thiolated primer or at least 40 ng/μl denatured amplicon were added to the suspension of AuNRs and incubated for two days at 4°C under constant agitation. In an attempt to reduce the electrostatic repulsion between the anionic AuNRs and the phosphate moieties of the nucleotides, a gradual addition of NaCl was performed until 1-1.4 M, according to the length of the thiolated sequence. Before use, AuNRs were washed four times to ensure the complete removal of unbound probes. The amount of each probe immobilized onto the AuNR surface was quantified by spectrophotometry at a wavelength of 260 nm, with reference to known concentrations of the individual components. Finally,

AuNRs were re-suspended in a hybridization buffer optimized for dot-blot assays at the nominal concentration of 0.8 mM Au.

Preparation of DNA targets and dot-blot assays

In order to assess the biomolecular recognition between the AuNR-labeled probes and specific target samples, a dot-blot assay was performed and compared to a standard method for labeling with digoxigenin (DIG-11-ddUTP, Roche Diagnostics, Germany) and detecting with an enzyme immunoassay [67].

1 μ l of each target was spotted onto positively charged nylon membranes and fixed for 3 min by an UV-crosslinker (Spectrolinker™ XL-1000 UV Crosslinker, Spectronics Corporation, USA). In order to establish the hybridization stringency, different oligonucleotides were immobilized in a range of concentration from 0.1 pM to 10 μ M, i.e. sequences complementary to the 21-mer oligonucleotide probe or featuring one or more mutations (base substitutions and/or deletions, see Table 1). The *rolC* fw primer and plain water were used as negative hybridization and contamination controls, respectively. In addition, the PCR product (1, 10 and 100 ng/ μ l) and plasmid DNA containing the *rolC* gene (1, 10, 50, 100, 200 ng/ μ l) were also spotted after thermal denaturation at 95°C for 10 min and rapid cooling in ice.

The DIG-labeled probe was prepared according to the instructions of the “DIG oligonucleotide 3'-end labeling” kit (2nd generation, Roche Diagnostics, Germany). A pre-hybridization of membranes was performed at 54°C for 30 min with an appropriate volume (20 ml/100 cm²) of a ready-to-use buffer (DIG Easy Hyb, Roche Diagnostics, Germany) in a hybridization oven (Techne®, UK). An overnight hybridization was then done at the same temperature with at least 3.5 ml/100 cm² DIG Easy Hyb buffer containing 200 pmol DIG-labeled probe. The next day, membranes were rinsed twice with a 2 \times saline-sodium citrate (SSC) solution supplemented with 0.1% sodium dodecyl sulfate (SDS) for 5 min at RT, followed by two high stringency washes in 0.1 \times SSC buffer with 0.1% SDS for 15 min at 65°C under constant agitation. The immunological detection was finally achieved by using an anti-digoxigenin antibody conjugated to alkaline phosphatase (AP), in the presence of the colorimetric substrates NBT/BCIP (4-nitroblue tetrazolium chloride/5-bromo-4-chloro-3-indolyl phosphate), as described in the procedure of the “DIG DNA labeling and detection” kit (Roche Diagnostics, Germany).

For colorimetric detection with the AuNRs, after pre-hybridization, membranes were incubated with relevant suspensions conjugated with the 41-mer or 328-mer sequences at the nominal concentration of 0.8 mM Au in DIG Easy Hyb buffer at 54°C under gentle agitation, until development of a visible color. Then, samples were just directed to post hybridization washes, rinsed with distilled water and air-dried.

Dot-blot setup for standardized measurements

In order to develop a reproducible system for quantitative analysis of the dot-blots based on an automated pipeline, additional membranes were prepared by using a system that was purposely

designed and produced by Ecobioservices and Researches (Italy), in collaboration with Laboratori Victoria (Italy).

First, nylon membranes with identical shape and size (3.6 cm × 3.6 cm) were created by using a custom-made cutter. Then, after thermal denaturation, serial dilutions of the purified *rolC* amplicon (from 10 to 0.1 ppm with a dilution factor of 4/3, and 0) were spotted onto these membranes in duplicate and in random order. In order to guarantee a uniform and reproducible deposition of all target samples and to minimize the variability due to manual pipetting, we implemented an appropriate dispenser (Figures 1a and S1a) made of a steel plate and a PMMA grid featuring 9 through-holes arranged in a 3 × 3 matrix. The steel plate includes a housing for the nylon membranes to settle in position. During dispensing, the PMMA grid was placed above the steel plate and its holes were used as a guide for a micropipette tip, in order to standardize the positions of the dots, and to streamline the subsequent analysis. A fine movement is available to control the distance between steel plate and PMMA grid. In this manner, each sample was set at a consistent pitch distance of its neighbors (about 0.9 cm).

As described above, membranes were UV-crosslinked, pre-hybridized and treated overnight with a suspension of AuNRs conjugated with the 41-mer oligonucleotide, at the nominal concentration of 0.4 mM Au. Low and high stringency washes were then carried out as usual. After air-drying, images of the dot-blot were captured using a digital camera mounted inside a darkroom designed to ensure a reproducible illumination and acquisition. The darkroom consists of a cabinet of a size of 15 cm × 15 cm base × 24.5 cm height and featuring a sealed door and a slot for correct insertion of the membranes (see Figures 1b and S1b). For uniform illumination, an array of 12 LEDs was installed around the digital camera in the upper wall of the cabinet. The camera was placed at a distance around 23 cm of the membranes and connected to a PC via USB. A custom-made software allows the user to control the intensity and RGB composition of the LEDs, and to acquire and store standardized photographs.

Analysis of dot-blot photographs by artificial intelligence

In order to check the feasibility to analyze the standardized photographs in the framework of a supervised machine-learning problem, we assessed the sensitivity of a pipeline that receives an image of a dot-blot membrane as input and returns a quantitative prediction of the concentration of the nucleotide target as output. The extreme limitation of the available dataset ($n = 36$ instances) imposed a strong reduction of its dimensionality, a preference for the simplest possible model, and a workflow circumventing the need to split it into train and test. Our objective was to understand the relevance of machine learning in our system, rather than to deploy an up-and-running predictor.

For dimensionality reduction, image segmentation and feature selection, photographs were first resized to greyscale and then preprocessed with a tool that leverages on the theoretical symmetry of the physical problem (see panel 5b). It consists of a mask made of 6 concentric rings, each of a Chebishev thickness of 6 px. In terms of physical size on the substrate, this corresponds to an outer diameter of 3.2 mm and distance from ring to ring of 270 μm , which approximately suit the max width of the dots and

the estimated lateral res of the imaging system. For each ring, the avg px intensity was computed, normalized to the value found at the outer edge of the mask and plotted vs numeral distance from the common center, i.e. from 0 to 5. These plots were also used to align the mask by fine-tuning its center around a nominal position, in a way to maximize their variance or, in other words, to minimize their blurriness. The assumption that this criterion optimizes the overlap with the physical pattern was checked by manual inspection. Therefore, each instance was reduced from a matrix of an approximate size of (70×70) px \times 3 colors $\sim 15 \times 10^3$ values to a vector of length $n = 6$ dimensions. Finally, in an attempt to further mitigate the effect of sample variance, each label was modified with a random tweak (5%) within the physical uncertainty of the pipette (at least 10%).

In order to deploy a supervised machine learning analysis, we used Scikit-learn [68] as a high-level environment comprising tools for performance assessment. In particular, we tested the simplest model of linear regressor and calculated its performance metrics with a cross-validation analysis implemented in a leave-one-out strategy, i.e. an extreme case of K-fold cross validation done with $K = n$. For each K-fold iteration, Scikit-learn provides both a test and a train error, which we compared for an overall assessment of its generalization error. We also used the cross-validation tool to generate so-called clean predictions, where the concentration of each instance was inferred from a sub-model trained with all other 35 cases. We examined these predictions to identify relevant trends vs true concentration, and to gain an indicative estimate of the sensitivity of our simple predictor. However, we declined to deploy and test a full regressor, because of too small a size of the available dataset.

Name	Sequence 5' > 3'	Use
41-mer oligonucleotide probe	Thiol-(CH ₂) ₆ -TTT TTT TTT TTT TTT TTT TTA TGG CTG AAG ACG ACC TGT GT	AuNR-probe, PCR primer
328-mer single-stranded probe	Thiol-(CH ₂) ₆ -TTT TTT TTT TTT TTT TTT TTT TTA TGG CTG AAG ACG ACC TGT GTT CTC TCT TTT TCA AGC TCA AAG TGG AGG ATG TGA CAA GCA GCG ATG AGC TAG CTA GAC ACA TGA AGA ACG CCT CAA ATG AGC GTA AAC CCT TGA TCG AGC CGG GTG AGA ATC AAT CGA TGG ATA TTG ACG AAG AAG GAG GGT CGG TGG GCC ACG GGC TGC TGT ACC TCT ACG TCG ACT GCC CGA CGA TGA TGC TCT GCT TCT ATG GAG GGT CCT TGC CTT ACA ATT GGA TGC AAG GCG CAC TCC TCA CCA ACC TTC CCC CGT ACC AGC ATG ATG TGA CTC TCG ATG A	AuNR-probe
<i>rolC</i> fw primer	ATG GCT GAA GAC GAC CTG TGT	PCR primer, target
<i>rolC</i> rev primer	TCA TCG AGA GTC ACA TCA TGC	PCR primer
DIG-labeled <i>rolC</i> fw primer	ATG GCT GAA GAC GAC CTG TGT-ddUTP-DIG	DIG-probe
<i>rolC</i> fw complementary sequence	ACA CAG GTC GTC TTC AGC CAT	Target
Mutated <i>rolC</i> fw complementary sequence_1	ACA CAG GTC GTC TTC AG - CAT	Target
Mutated <i>rolC</i> fw complementary sequence_2	ACA CAG GTC TTC TTC AG - CAT	Target
Mutated <i>rolC</i> fw complementary sequence_3	ACA CAG GTC TTC TTC CG - CAT	Target

Table 1: DNA sequences used as molecular probes and targets for the dot-blot assays and as PCR primers for *roIC* gene amplification. All mutated complementary sequences include one deletion (-) plus none, one (G>T) or two (G>T; A>C) base substitutions.

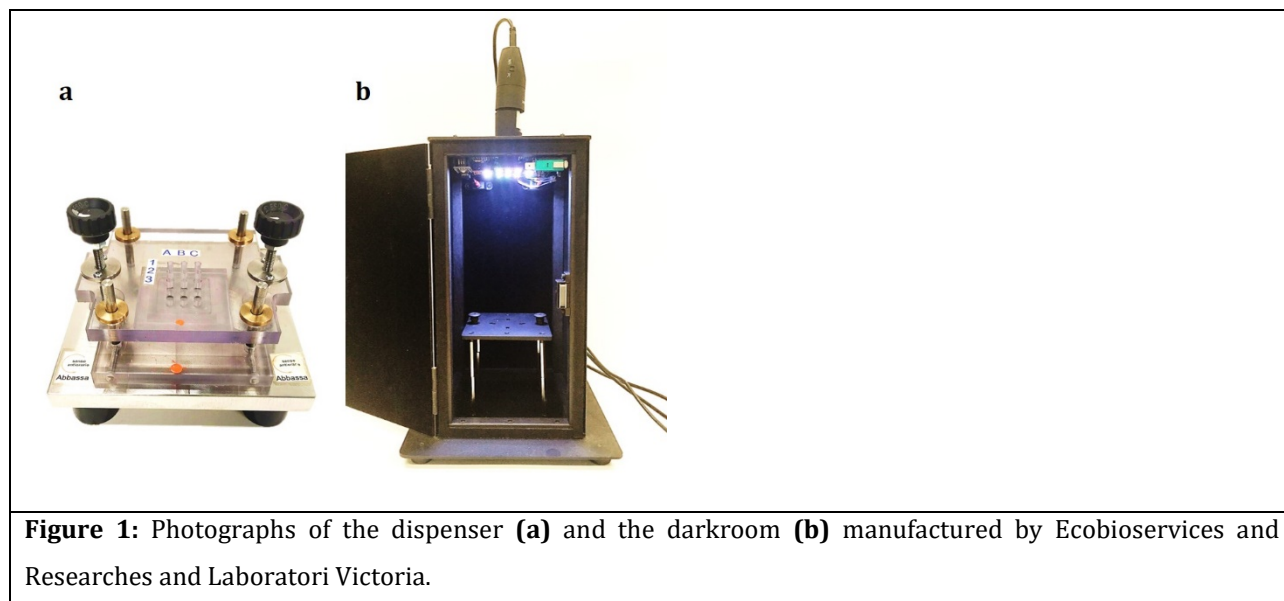


Figure 1: Photographs of the dispenser **(a)** and the darkroom **(b)** manufactured by Ecobioservices and Researches and Laboratori Victoria.

Results and Discussion

Characterization of citrate-AuNRs

By being a cationic surfactant, CTAB is widely used in extraction buffers to facilitate the purification of DNA from polysaccharides and pigments in plant tissues [69–71]. Thus, in order to avoid a non-specific immobilization of oligonucleotides on the surface of the particles, and their flocculation, due to electrostatic interactions, cetrimonium-AuNRs were gradually converted into citrate-AuNRs.

The electrokinetic potential and hydrodynamic size of citrate-AuNRs were analyzed by DLS and compared to their as-synthesized cetrimonium-stabilized counterpart. To perform these measurements, AuNRs were diluted in ultrapure water until a nominal concentration of 80 μM Au. The mean values of their ζ potential and average diameter changed from $(+30.9 \pm 3.0)$ to (-28.4 ± 2.1) mV and from (100.2 ± 3.9) to (98.1 ± 3.4) nm. The optical spectra of the AuNRs displayed two characteristic peaks: a longitudinal band centered around 790 nm and a transversal one about 516 nm. As shown in Figure 2a, the extinction spectra of the colloids coated with citrate or cetrimonium were almost indistinguishable. When subjected to a 1% agarose gel electrophoretic run, 3.6 mM Au citrate-AuNRs migrated towards the anode for a distance around 1.5 cm in 0.5 \times Tris-Borate EDTA buffer (TBE, pH 8.3) at 100 V for 60 min (Figure 2b, sample 2). On the other hand, cetrimonium-AuNRs failed to leave their well, probably due to the onset of flocculation under the ionic strength of the TBE buffer (sample 1). (Note that the pore size of a 1% agarose gel was estimated to range from 100 to 500 nm [72, 73]). Taken together, these data demonstrate the successful replacement of CTAB with Na_3 -citrate, while preserving the colloidal stability and optical properties of the AuNRs. We found that these colloids remain stable and usable for several months when stored at shelf conditions.

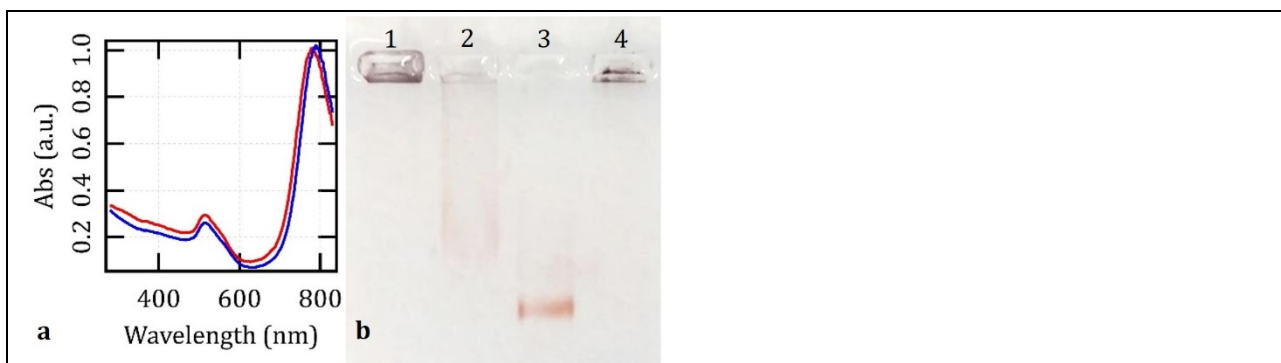


Figure 2: **a)** Representative optical spectra of AuNRs at the nominal concentration of 160 μM Au in 0.5 mM CTAB and 0.005% Tween® 20 (blue) or in 5 mM $\text{Na}_3\text{-citrate}$ (red). **b)** Electrophoretic mobility of cetrimonium-AuNRs (1), citrate-AuNRs (2) and citrate-AuNRs functionalized with the 41-mer oligonucleotide (3) or the 328-mer single-stranded sequence (4) in 1% agarose gel under 100 V for 60 min in TBE buffer.

Characterization of the bioconjugated AuNRs



Figure 3: **a)** Representative images of 0.8 mM Au citrate-AuNRs. 1) control particles, 2) AuNRs functionalized with the 41-mer oligonucleotide + NaCl, 3) AuNRs conjugated to the 328-mer single-stranded fragment + NaCl, 4) control particles + NaCl. **b-e)** Control AuNRs (1) and AuNRs conjugated to the 41-mer oligonucleotide (2) resuspended in DIG Easy Hyb buffer (b: 5 min and c: 24 hours) or in DPBS (d: 3 hours) at a nominal concentration of 0.8 mM Au at RT, and in a typical PCR master mix at a rate of 1.6 mM Au after 25 thermal cycles (e).

High concentrations of NaCl proved to be essential to mitigate the electrostatic repulsion between the citrate-AuNRs and the thiolated sequences, and to promote a proper functionalization. In order to avoid destabilizing the suspension, salt was added in small aliquots at regular intervals over 2 days. While the bioconjugation progressed, the color of the AuNRs became even more crimson and brilliant (Figure 3a, sample 2) than the control colloids (Figure 3a, sample 1). We ascribe this change to the increase of the refractive index of saline from 1.333 until 1.344 as salt reaches a concentration of 1 M [74], and/or to a high density of surface-bound oligonucleotides. In the case of the 328-mer probe (Figure 3a, sample 3), there occurred some particle aggregation, probably due to the higher concentration of NaCl that was

needed to overcome the stronger repulsion (1.4 M). In the absence of any thiolated sequence, citrate-AuNRs underwent massive and irreversible flocculation while dosing NaCl (Figure 3a, sample 4).

The mean loading capacity of the 41-mer or the 328-mer probes on 0.8 mM Au AuNRs was quantified by spectrophotometry, and it was around 500 nM (corresponding to about 200 macromolecules per particle) and 16 ng/ μ l (i.e., about 80 nM, or 30 macromolecules per particle, which is in line with the typical rate of immobilizable immunoglobulins [9]), respectively. Even if no significant difference was observed in terms of ζ potential and size, AuNRs functionalized with the 41-mer oligonucleotide displayed even greater electrophoretic mobility in TBE buffer than control particles (Figure 2b, sample 3). In fact, these particles migrated by about 2 cm towards the anode, with respect to 1.5 cm for the bare citrate-AuNRs, when exposed to 100 V for 60 min in 1% agarose gel, and their band was much narrower. Instead, when scanned by DLS, the AuNRs labelled with the 328-mer probe returned a hydrodynamic size around 157.4 ± 5.1 nm and signs of microscopic aggregation. The onset of aggregation in this colloid may be the main reason why it remained in its well during gel electrophoresis (Figure 2b, sample 4).

Both the shorter and the longer sequences also stabilized the citrate-AuNRs in saline buffers or at high temperatures (Figure 3, b-e). The control sample visibly changed in color within few min after resuspension in DIG Easy Hyb buffer (b) and completely flocculated after 24 hours (c) at room temperature. The aggregation of citrate-AuNRs usually started after 3 hours in DPBS (d). They also showed instability after 25 thermal cycles of a standard PCR run (e). In contrast, the bioconjugated AuNRs successfully endured all these quality tests.

Dot-blot analysis

With the aim to establish a new rapid colorimetric sensor based on citrate-AuNRs functionalized with single-stranded DNA sequences of different length, a dot-blot assay was performed and compared against a gold-standard method for labeling and detection. Digoxigenin is a steroid hapten that is in common use to label DNA probes for hybridization to membrane-blotted nucleic acids, according to standard methods [75]. The molecular hybrids are then immunodetected with anti-digoxigenin antibodies coupled to AP, and revealed with the colorimetric substrates NBT/BCIP.

First, the hybridization stringency was assessed by immobilizing decreasing concentrations (from 10 μ M to 0.1 pM) of target sequences point-mutated or fully complementary to the 21-mer probe labelled with digoxigenin or AuNRs. The *rolC* forward primer was used as negative control in each membrane. All samples were prepared in duplicate to validate the reproducibility of the signals. As shown in Figure S2 in Additional file 1, colored dots appeared only after hybridization between the oligonucleotide probe and its fully complementary sequence (line B) at 0.1 (B3, B4) and 1 nM (B1, B2). A single nucleotide deletion in this target was enough to prevent the development of any visible signal (line C), just as the further addition of one (line D) and two (line E) substitutions, even at the highest concentrations. No color emerged in the case of plain water, which rules out the effect of contaminations (column n. 11).

A high specificity of hybridization was also observed when labeling was made with AuNRs. Dots clearly appeared for concentrations exceeding 10 nM of the sequence fully complementary to the *rolC* fw primer (Figure 4a, line A), and no signal arose from the mutated targets (Figure 4a, lines B and C) nor from the negative control (Figure 4a, line D).

In addition, the DIG-labelled probe enabled the recognition of the pUC19 plasmid containing the *rolC* transgene at 1, 10 and 50 ng/ μ l (Figure S2 in Additional file 1, F1–F6). Since the *rolC* sequence amounts to approximately 7% of the entire cloning vector, the minimum detectable concentration was about 70 pg/ μ l. Moreover, the intensity of the spots increased with the concentration of the target.

AuNRs conjugated to the 41-mer oligonucleotide allowed to easily identify the *rolC* amplicon until 1 ng/ μ l (Figure 4b, line C). However, it took as much as 50 ng/ μ l of pUC19::*rolC* plasmid to raise a signal with this tag (Figure 4b, D1). Also in this membrane, different concentrations of *rolC* fw primer and its complementary sequence were used as negative (line B) and positive (line A) controls, respectively.

In an attempt to enhance the sensitivity of detection of the plasmid DNA, we tested the use of the AuNRs conjugated to the 328-mer single-stranded sequence. By doing so, the detection limit decreased by about five folds down to 10 ng/ μ l, which corresponds to 0.7 ng/ μ l of *rolC* transgene, in this kind of sample (Figure 4c, A3). Equal concentrations of *rolC* amplicon were much more clearly visible when the AuNRs were conjugated to a longer probe (Figure 4c, line B).

Our results demonstrate that labelling with AuNRs allows the detection of small amounts of DNA targets. Despite a lower sensitivity with respect to the gold-standard digoxigenin, AuNRs provide much better speed and ease of use. When using AuNRs, a visible coloration already emerges within about 10 min of incubation, and saturates after few hours. Furthermore, AuNRs drastically streamline the steps and costs of the analytical protocol. After hybridization and standard stringency washes, the use of digoxigenin entails the preparation and implementation of blocking, antibody and color-substrate solutions, thus exploding the complexity of the workflow. The blocking and antibody solutions require a minimum of 30 min each. Then, after a washing step, the membrane must be incubated with the detection buffer for several hours in the dark. In fact, the colorimetric reaction starts within several minutes and saturates after 16 hours, for reliable readout. Furthermore, the blocking and color-substrate solutions must be prepared as fresh as possible each time, and the antibody one is usable only within 12 hours when stored at 2-8°C. On the other end, the use of AuNRs allows real-time monitoring of the process of hybridization by the naked eye, because the hybridized probe is directly bound to the colorimetric tag. No preparation of buffers nor particular solutions are needed, but only post-hybridization washes may be desirable for more accurate use. If carefully stored at 4°C, the same suspension of bioconjugated AuNRs is reusable multiple times over several weeks, without visible loss of colloidal stability nor staining efficiency. As a whole, the approach based on AuNRs is much less expensive than that relying on digoxigenin, and may enable new applications, such as e.g. real-time monitoring of the process of hybridization under dynamic conditions.

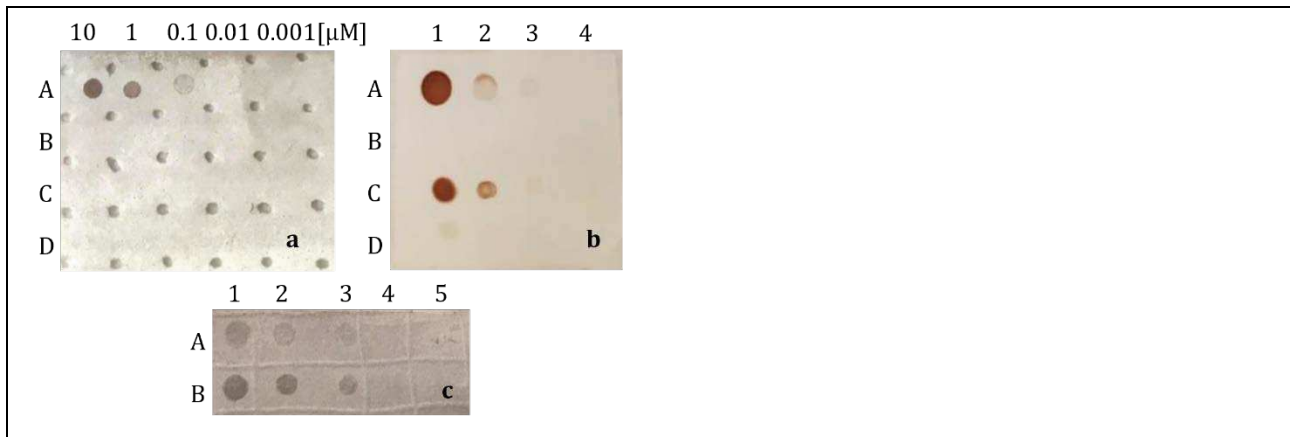


Figure 4: a) Evaluation of the hybridization stringency between the 41-mer oligonucleotide bound to the AuNRs and its complementary sequence (A) spotted onto a nylon membrane. Targets with just two (B) or three (C) point mutations or completely identical to the oligonucleotide probe (D) did not allow any coloration to develop. **b)** Colorimetric detection of the sequence complementary to the *roIC* fw primer used as positive control (A: 10, 1, 0.1, 0 μM), *roIC* fw primer as negative control (B: 10, 1, 0.1, 0 μM), *roIC* amplicon (C: 100, 10, 1, 0 ng/μl) and pUC19::*roIC* plasmid (D: 50, 10, 1, 0 ng/μl) by means of AuNRs functionalized with the 41-mer oligonucleotide. **c)** Dot-blot assay of plasmid DNA containing the *roIC* gene (A: 200, 100, 10, 1, 0 ng/μl) and *roIC* amplicon (B: 100, 10, 1, 0 ng/μl) by implementing AuNRs functionalized with the 328-mer probe.

Quantitative system for dot-blot image analysis

Together with the development of the plasmonic material, we tested the feasibility of a supervised machine learning paradigm to obtain quantitative predictions of the concentration of the target analyte from a photograph of a dot-blot assay.

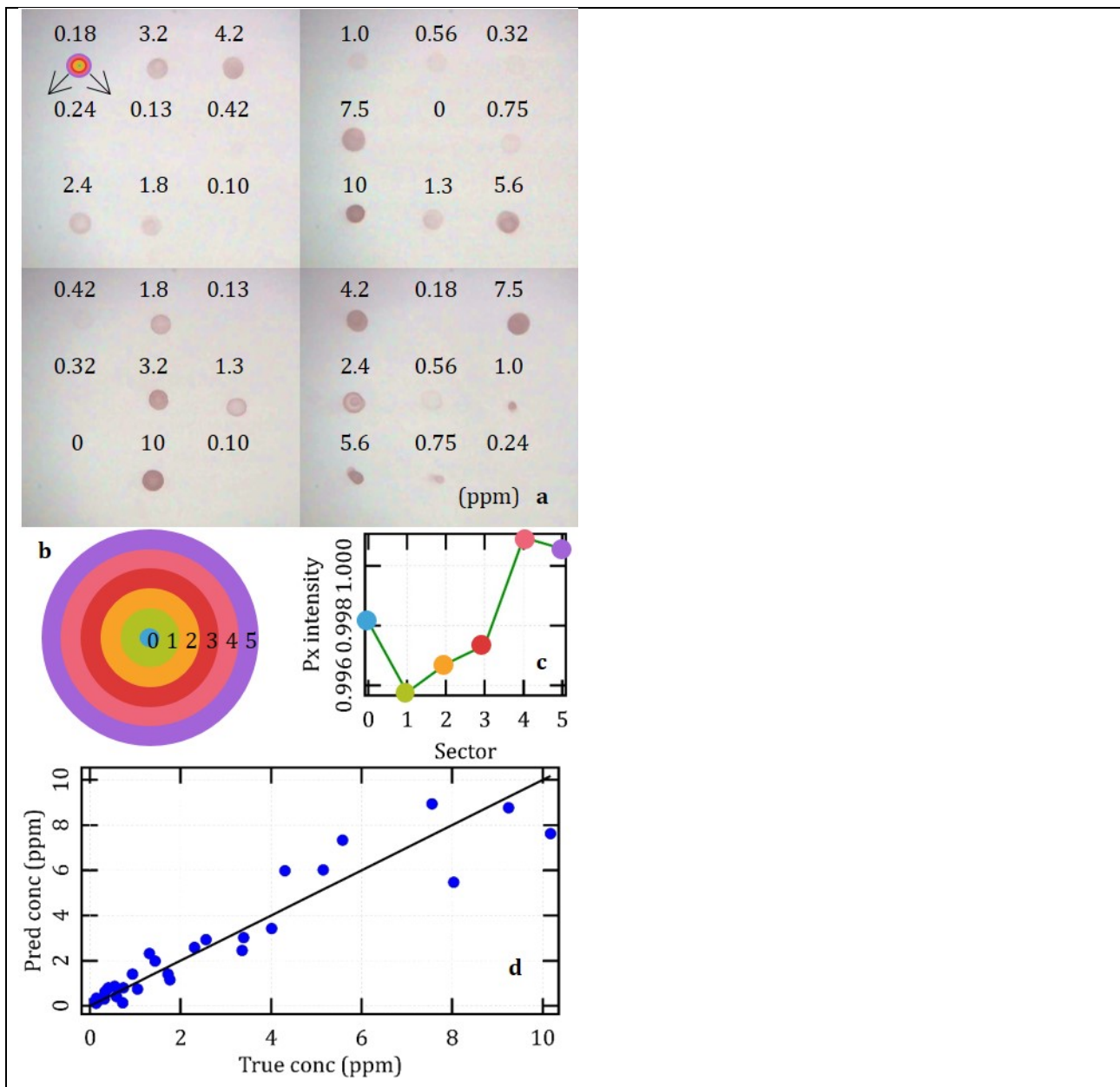


Figure 5: **a)** standardized photographs of the entire data set of dot-blots. The multi-colored circle in the upper left corner is the mask used for feature selection, in full scale; **b)** close-up of the mask highlighting its concentric layout; **c)** example of an instance preprocessed with the mask. This case is a dot-blot corresponding to a target concentration of 0.24 ppm, which is invisible to the naked eye, but unveils a significant pattern upon feature selection; **d)** results achieved with the cross-validation regressors based on a simple linear model, and expressed in terms of predicted vs true target concentration.

Figure 5 represents the preliminary pipeline that we implemented to automate the analysis of our dot-blots. According to the photographs shown in Panel 5a, dots come in irregular combinations of size and shape, sometimes featuring multiple coffee rings [76], but altogether exhibit some pattern to the concentration of the target analyte. In particular, there appears to be a consistent trend for instances corresponding to densities exceeding about 1.0 ppm. Instead, nothing is clearly visible to the naked eye below 0.42 ppm. Panels 5a to c illustrate our procedure for feature selection based on averaging over

consecutive rings. As an example, panel 5c refers to the bottom-rightmost instance in panel 5a and suggests that it may help expose subtle patterns that may elude a qualitative inspection. Panel 5d summarizes the results achieved by applying a cross-validation approach based on a simple linear regressor. We recall that our estimates are clean predictions, in that each one derives from a leave-one-out regressor trained with the other 35 instances. In turn, this also means that our graph actually displays results obtained from 36 different predictors, i.e. it is not a full model.

The cross-validation predictions feature a mean absolute error (MAE) with respect to the true labels of 0.59 ppm. However, it turns out that the discrepancy tends to decrease with concentration, in absolute terms (see Figure S3 in Additional file 1). For instance, over the range from 0 to 1 ppm, it amounts to a MAE of 0.24 ppm, which may be considered as an indicator of the detection limit and sensitivity of our demonstrator. In relative terms, we note that metrics tend to improve with concentration, though. Above 2 ppm, the relative error tends to converge to an average value around 19% (see Figure S3).

Our results collectively prove the feasibility of an approach based on a supervised machine learning pipeline to obtain a quantitative readout of our dot-blot. Meanwhile, with respect to an assay based on a visual assessment, it holds the potential to tweak its detection limit by about two folds, say from around 0.42 to 0.24 ppm. We also note that the average of the mean absolute train errors of our cross-validation regressors amounts to 0.40 ppm, which is about 30% lower than their mean absolute test errors, as reported above, thus pointing to a systematic tendency to overfit their respective input datasets. Therefore, since the linear assumption is already likely to oversimplify the physical process, thus bearing some bias, we expect that a larger dataset will allow much better predictions, and the possibility to test hyperparametric models. Another improvement may come from a refinement of the system hardware and all methods for standardized imaging. Panel 5a clearly shows that there remains further scope to optimize the alignment of the dot-blot and the illumination of the substrate. Overall, we are confident that a sensitivity below 0.1 ppm will probably be targetable without too much effort.

Conclusions

In conclusion, we have conjugated citrate-terminated gold nanorods with two different DNA probes and implemented a setup that pursues a rapid, accurate and reproducible method of detection of a genetic target. Although the use of gold nanorods implies a lower sensitivity than the gold-standard method based on digoxigenin, our system may be enough for use in critical contexts like the diagnosis of most infectious diseases, where the pathogen concentration is relatively high. It works fine with a model target, as well as PCR products and plasmid DNA, and it is stringent against single point mutations. The main advantage is a much more streamlined procedure, which may also open new possibilities, like the real-time observation of biorecognition events occurring under dynamic conditions.

We have also discussed the perspective to analyze the dot-blot membranes with a supervised machine learning approach implemented after a dedicated methodology for the acquisition of standardized photographs. A simple linear regressor built over a dataset of as few as 36 dots already returned leave-

one-out cross-validation predictions with a MAE of 0.59 ppm, which decreases to 0.24 ppm in the range of concentration of the target analyte below 1 ppm. These results are rather surprising, when it is considered that the starting point was a naked-eye detection limit around 0.42 ppm, and that the entire pipeline from system hardware for standardized imaging to the accumulation of an adequate training dataset and the optimization of the regression model leaves substantial room for improvement.

In conclusion, our work provides clear clues for the enhancement of paper-based assays by implementing a holistic combination of synergistic adjustments: 1) the use of gold nanorods rather than standard spherical particles, which proves to be feasible, and constitutively conveys about 10× brightness; 2) the optimization of a genetic strategy, where we have reported our case of a 5× reduction of the detection limit of a transgene cloned into a plasmid, whose sequence represents about 7% of the entire vector, by simply tuning the probe chain length; and 3) the implementation of a pipeline for quantitative readout based on machine learning, where a preliminary test was already enough to yield another 2× sensitivity. Taken together, we are confident that our work will inspire a redesign of important tools like the so-called rapid antigen-tests for SARS-CoV-2, where the incorporation of recent advances in nanobiotechnology and data processing may really boost the analytical performances to the level of lab-grade methods.

Supplementary Information

The online version contains supplementary material available at...

Additional file 1: additional details on the experimental setup; the use of a DIG-labeled probe as gold-standard reference for the dot-blot assays; and on the analysis of the absolute errors of the cross validation predictors.

Authors' contributions

CB and S_{Ce} prepared the particles and interpreted all data; S_{Ce}, PB and FR conceived the work; S_{Ch} and PB prepared the genetic material; CB, S_{Ch} and PB performed dot-blot assays; FM and MG standardized the protocols for image acquisition; PG, SL and FT developed the hardware and software for standardized imaging; AB, NZ and FR deployed the machine learning analysis; RP and FR supervised the work; all authors contributed to manuscript preparation. All authors read and approved the final manuscript.

Funding

This work was partially supported by Tuscany Region through Project “THERMINATOR” (Call on Health Bando Ricerca Salute 2018) and Project “SENSOGM” (POR FESR Toscana 2014-2020), Tuscany Region and European Commission through Horizon 2020 ERANET-Cofund Project “PLABAN” (Call

PhotonicSensing), and by a collaborative grant from National Research Council Italy and Russian Foundation for Basic Research (18-52-7803, “HYPNOSIS”)

Availability of data and materials

All data are available from the corresponding author on reasonable request.

Declarations

Consent for publication

Written informed consent for publication was obtained from all participants.

References

1. Mieszawska AJ, Mulder WJ, Fayad ZA, Cormode DP. Multifunctional gold nanoparticles for diagnosis and therapy of disease. *Mol Pharm*. 2013;10(3):831–47. doi:10.1021/mp3005885.
2. Kohout C, Santi C, Polito L. Anisotropic Gold Nanoparticles in Biomedical Applications. *Int J Mol Sci*. 2018;19(11):3385. doi:10.3390/ijms19113385.
3. Yu L, Song ZS, Peng J, Yang M, Zhi H, He H. Progress of gold nanomaterials for colorimetric sensing based on different strategies. *TrAC Trends in Analytical Chemistry* 2020;127:115880. <https://doi.org/10.1016/j.trac.2020.115880>.
4. Pylaev T, Avdeeva E, Khlebtsov N. Plasmonic nanoparticles and nucleic acids hybrids for targeted gene delivery, bioimaging, and molecular recognition. *Journal of Innovative Optical Health Sciences* 2021;14(4):2130003. <https://doi.org/10.1142/S1793545821300032>.
5. Ratto F, Matteini P, Centi S, Rossi F, Pini R. Gold nanorods as new nanochromophores for photothermal therapies. *Journal of Biophotonics* 2011;4(1-2):64–73. <https://doi.org/10.1002/jbio.201000002>.
6. Jain PK, Lee KS, El-Sayed IH, El-Sayed MA. Calculated absorption and scattering properties of gold nanoparticles of different size, shape, and composition: applications in biological imaging and biomedicine. *J Phys Chem B*. 2006;110(14):7238–48. doi:10.1021/jp057170o.
7. Ghosh SK, Pal T. Interparticle coupling effect on the surface plasmon resonance of gold nanoparticles: from theory to applications. *Chem. Rev*. 2007;107:4797–4862. doi:10.1021/CR0680282.
8. Aubin-Tam M-E. Conjugation of nanoparticles to proteins. *Methods Mol Biol*. 2013;1025:19–27. doi:10.1007/978-1-62703-462-3_3.
9. Centi S, Ratto F, Tatini F, Lai S, Pini R. Ready-to-use protein G-conjugated gold nanorods for biosensing and biomedical applications. *J Nanobiotechnology*. 2018;16(1):5. doi:10.1186/s12951-017-0329-7.
10. Centi S, Tatini F, Ratto F, Gnerucci A, Mercatelli R, Romano G, et al. In vitro assessment of antibody-conjugated gold nanorods for systemic injections. *J Nanobiotechnology*. 2014;12:55. doi:10.1186/s12951-014-0055-3.
11. Jazayeri MH, Amani H, Pourfatollah AA, Pazoki-Toroudi H, Sedighimoghaddam B. Various methods of gold nanoparticles (GNPs) conjugation to antibodies. *Sensing and Bio-Sensing Research*. 2016;9:17–22. <https://doi.org/10.1016/j.sbsr.2016.04.002>.
12. Akbarzadeh Khiavi M, Safary A, Aghanejad A, Barar J, Rasta SH, Golchin A, et al. Enzyme-conjugated gold nanoparticles for combined enzyme and photothermal therapy of colon cancer cells. *Colloids and Surfaces A: Physicochemical and Engineering Aspects*. 2019;572:333–344. <https://doi.org/10.1016/j.colsurfa.2019.04.019>.

13. Wang Y, van Asdonk K, Zijlstra P. A robust and general approach to quantitatively conjugate enzymes to plasmonic nanoparticles. *Langmuir*. 2019;35(41):13356–13363. <https://doi.org/10.1021/acs.langmuir.9b01879>.
14. Zhang J, Liu B, Liu H, Zhang X, Tan W. Aptamer-conjugated gold nanoparticles for bioanalysis. *Nanomedicine (Lond)*. 2013;8(6):983–93. doi:10.2217/nnm.13.80.
15. Dorraj GS, Rassaei MJ, Latifi AM, Pishgoo B, Tavallaei M. Selection of DNA aptamers against Human Cardiac Troponin I for colorimetric sensor based dot blot application. *J Biotechnol*. 2015;208:80–6. doi:10.1016/j.jbiotec.2015.05.002.
16. Li J, Zhu B, Yao X, Zhang Y, Zhu Z, Tu S, et al. Synergetic approach for simple and rapid conjugation of gold nanoparticles with oligonucleotides. *ACS Appl Mater Interfaces*. 2014;6(19):16800–7. doi:10.1021/am504139d.
17. Jamdagni P, Khatri P, Rana JS. Nanoparticles based DNA conjugates for detection of pathogenic microorganisms. *Int Nano Lett*. 2016;6:139–146. <https://doi.org/10.1007/s40089-015-0177-0>.
18. Wang CH, Chang CW, Peng CA. Gold nanorod stabilized by thiolated chitosan as photothermal absorber for cancer cell treatment. *Journal of Nanoparticle Research*. 2011;13:2749–2758. <https://doi.org/10.1007/s11051-010-0162-5>.
19. Lopes LC, Lima D, Mendes Hacke AC, Schweigert BS, Calaça GN, Simas FF, et al. Gold nanoparticles capped with polysaccharides extracted from pineapple gum: Evaluation of their hemocompatibility and electrochemical sensing properties. *Talanta*. 2021;223:121634. <https://doi.org/10.1016/j.talanta.2020.121634>.
20. Armanetti P, Chillà A, Margheri F, Biagioni A, Menichetti L, Margheri G, et al. Enhanced Antitumoral Activity and Photoacoustic Imaging Properties of AuNP-Enriched Endothelial Colony Forming Cells on Melanoma. *Adv. Sci*. 2020;8(4):2001175. doi:10.1002/advs.202001175.
21. Puertas S, Moros M, Fernández-Pacheco R, Ibarra MR, Grazú V, de la Fuente JM. Designing novel nano-immunoassays: antibody orientation versus sensitivity. *J. Phys. D: Appl. Phys*. 2010;43(47):474012. doi:10.1088/0022-3727/43/47/474012.
22. Li H, Rothberg L. Colorimetric detection of DNA sequences based on electrostatic interactions with unmodified gold nanoparticles. *PNAS*. 2004;101(39):14036–14039. <https://doi.org/10.1073/pnas.0406115101>.
23. Chatterjee K, Kuo CW, Chen A, Chen P. Detection of residual rifampicin in urine via fluorescence quenching of gold nanoclusters on paper. *J Nanobiotechnol*. 2015;13:46. <https://doi.org/10.1186/s12951-015-0105-5>.
24. Cheng S, Tian J, Zheng B, Wei H, Ding Y, Zhao J. Paper-based readout to improve the measuring accuracy of gold nanoparticle aggregation-based colorimetric biosensors. *Anal. Methods*. 2017;9:5407–5413. <https://doi.org/10.1039/C7AY01683B>.
25. de la Rica R, Stevens MM. Plasmonic ELISA for the detection of analytes at ultralow concentrations with the naked eye. *Nat Protoc*. 2013;8:1759–1764. <https://doi.org/10.1038/nprot.2013.085>.
26. Bui M-P N, Ahmed S, Abbas A. Single-digit pathogen and attomolar detection with the naked eye using liposome-amplified plasmonic immunoassay. *Nano Lett*. 2015;15(9):6239–6246. <https://doi.org/10.1021/acs.nanolett.5b02837>.
27. Liu H, Rong P, Jia H, Yang J, Dong B, Dong Q, et al. A Wash-Free Homogeneous Colorimetric Immunoassay Method. *Theranostics*. 2016;6(1):54–64. doi:10.7150/thno.13159.
28. Koczula KM, Gallotta A. Lateral flow assays. *Essays in Biochemistry*. 2016;60:111–120. doi:10.1042/EBC20150012.

29. Kim H, Chung D-R, Kang M. A new point-of-care test for the diagnosis of infectious diseases based on multiplex lateral flow immunoassays. *Analyst*. 2019;144:2460–2466. <https://doi.org/10.1039/C8AN02295J>.
30. Joseph V, Matschulat A, Polte J, Rolf S, Emmerling F, Kneipp J. SERS enhancement of gold nanospheres of defined size. *J. Raman Spectrosc*. 2011;42:1736–1742. <https://doi.org/10.1002/jrs.2939>.
31. Jääskeläinen AE, Ahava MJ, Jokela P, Szivovics L, Pohjala S, Vapalahti O, et al. Evaluation of three rapid lateral flow antigen detection tests for the diagnosis of SARS-CoV-2 infection. *J Clin Virol*. 2021;137:104785. doi:10.1016/j.jcv.2021.104785.
32. Kim D, Lee J, Bal J, Seo SK, Chong CK, Lee JH, et al. Development and Clinical Evaluation of an Immunochromatography-Based Rapid Antigen Test (GenBody™ COVAG025) for COVID-19 Diagnosis. *Viruses*. 2021;13(5):796. doi:10.3390/v13050796.
33. Bordi L, Sberna G, Lalle E, Piselli P, Colavita F, Nicastrì E, et al. Frequency and Duration of SARS-CoV-2 Shedding in Oral Fluid Samples Assessed by a Modified Commercial Rapid Molecular Assay. *Viruses*. 2020;12(10):1184. <https://doi.org/10.3390/v12101184>.
34. Aveyard J, Mehrabi M, Cossins A, Braven H, Wilson R. One step visual detection of PCR products with gold nanoparticles and a nucleic acid lateral flow (NALF) device. *Chem. Commun*. 2007;4251–4253. doi:10.1039/b708859k.
35. Nagatani N, Yamanaka K, Ushijima H, Koketsu R, Sasaki T, Ikuta K, et al. Detection of influenza virus using a lateral flow immunoassay for amplified DNA by a microfluidic RT-PCR chip. *Analyst*. 2012;137(15):3422–6. doi:10.1039/c2an16294f.
36. Nihonyanagi S, Kanoh Y, Okada K, Uozumi T, Kazuyama Y, Yamaguchi T, et al. Clinical usefulness of multiplex PCR lateral flow in MRSA detection: a novel, rapid genetic testing method. *Inflammation*. 2012;35(3):927–34. doi:10.1007/s10753-011-9395-4.
37. Prompamorn P, Sithigorngul P, Rukpratanporn S, Longyant S, Sridulyakul P, Chaivisuthangkura P. The development of loop-mediated isothermal amplification combined with lateral flow dipstick for detection of *Vibrio parahaemolyticus*. *Lett Appl Microbiol*. 2011;52(4):344–51. doi:10.1111/j.1472-765X.2011.03007.x.
38. Roskos K, Hickerson AI, Lu HW, Ferguson TM, Shinde DN, Klaue Y, et al. Simple system for isothermal DNA amplification coupled to lateral flow detection. *PLoS One*. 2013;8(7):e69355. doi:10.1371/journal.pone.0069355.
39. Jauset-Rubio M, Svobodová M, Mairal T, McNeil C, Keegan N, Saeed A, Abbas MN, et al. Ultrasensitive, rapid and inexpensive detection of DNA using paper based lateral flow assay. *Sci Rep* 2016;6:37732. <https://doi.org/10.1038/srep37732>.
40. Bulgakov VP, Shkryl YN, Veremeichik GN, Gorpenchenko TY, Inyushkina YV. Application of *Agrobacterium* *rol* Genes in Plant Biotechnology: A Natural Phenomenon of Secondary Metabolism Regulation. In: Alvarez M, editor. *Genetic Transformation*. IntechOpen; 2011. doi:10.5772/24200.
41. Bulgakov VP. Functions of *rol* genes in plant secondary metabolism. *Biotechnology Advances*. 2008;26(4):318–324. doi:10.1016/j.biotechadv.2008.03.001.
42. Bogani P, Liò P, Intrieri MC, Buiatti M. A physiological and molecular analysis of the genus *Nicotiana*. *Mol Phylogenet Evol*. 1997;7:62–70. doi:10.1006/mpev.1996.0356.
43. Intrieri MC, Buiatti M. The horizontal transfer of *Agrobacterium* *rhizogenes* genes and the evolution of the genus *Nicotiana*. *Mol Phylogenet Evol*. 2001;20:100–10. doi:10.1006/mpev.2001.0927.
44. Aoki S, Syōno K. Horizontal gene transfer and mutation: *Ngrol* genes in the genome of *Nicotiana glauca*. *Proc Natl Acad Sci USA*. 1999;96(23):13229–34. <https://doi.org/10.1073/pnas.96.23.13229>.

45. Hu M, Chen J, Li ZY, Au L, Hartland GV, Li X, et al. Gold nanostructures: engineering their plasmonic properties for biomedical applications. *Chem Soc Rev*. 2006;35(11):1084–94. doi:10.1039/b517615h.
46. Ratto F, Matteini P, Cini A, Centi S, Rossi F, Fusi F, et al. CW laser-induced photothermal conversion and shape transformation of gold nanodogbones in hydrated chitosan films. *Journal of Nanoparticle Research* 2011;13:4337–4348. doi:10.1007/s11051-011-0380-5.
47. Huff TB, Tong L, Zhao Y, Hansen MN, Cheng JX, Wei A. Hyperthermic effects of gold nanorods on tumor cells. *Nanomedicine*. 2007;2(1):125–132. doi:10.2217/17435889.2.1.125.
48. Hauck TS, Jennings TL, Yatsenko T, Kumaradas JC, Chan WCW. Enhancing the Toxicity of Cancer Chemotherapeutics with Gold Nanorod Hyperthermia. *Adv. Mater*. 2008;20:3832–3838. <https://doi.org/10.1002/adma.200800921>.
49. Manohar S, Ungureanu C, Van Leeuwen TG. Gold nanorods as molecular contrast agents in photoacoustic imaging: the promises and the caveats. *Contrast Media Mol. Imaging* 2011;6:389–400. <https://doi.org/10.1002/cmmi.454>.
50. Ratto F, Witort E, Tatini F, Centi S, Lazzeri L, Carta F, et al. Plasmonic Particles that Hit Hypoxic Cells. *Adv. Funct. Mater*. 2015;25(2):316–323. <https://doi.org/10.1002/adfm.201402118>.
51. Ratto F, Centi S, Avigo C, Borri C, Tatini F, Cavigli L, et al. A Robust Design for Cellular Vehicles of Gold Nanorods for Multimodal Imaging. *Advanced Functional Materials* 2016;26(4):7954–7954. <https://doi.org/10.1002/adfm.201600836>.
52. Mehtala JG, Zemlyanov DY, Max JP, Kadasala N, Zhao S, Wei A. Citrate-Stabilized Gold Nanorods. *Langmuir*. 2014;30:13727–13730. [dx.doi.org/10.1021/la5029542](https://doi.org/10.1021/la5029542).
53. Wang J, Thomas M, Lin P, Cheng JX, Matei DE, Wei A. siRNA Delivery Using Dithiocarbamate-Anchored Oligonucleotides on Gold Nanorods. *Bioconjug Chem*. 2019;30(2):443–453. doi:10.1021/acs.bioconjchem.8b00723.
54. Khlebtsov B, Khlebtsov N. Surface-Enhanced Raman Scattering-Based Lateral-Flow Immunoassay. *Nanomaterials (Basel)*. 2020;10(11):2228. doi:10.3390/nano10112228.
55. Yan S, Liu C, Fang S, Ma J, Qiu J, Xu D, et al. SERS-based lateral flow assay combined with machine learning for highly sensitive quantitative analysis of Escherichia coli O157:H7. *Anal Bioanal Chem*. 2020;412(28):7881–7890. doi:10.1007/s00216-020-02921-0.
56. Jo YJ, Cho H, Lee SY, Choi G, Kim G, Min H, et al. Quantitative Phase Imaging and Artificial Intelligence: A Review. *IEEE Journal of Selected Topics in Quantum Electronics*. 2019;25(1):1–14. doi:10.1109/JSTQE.2018.2859234.
57. Oszwald A, Wasinger G, Pradere B, Shariat SF, Comp erat EM. Artificial intelligence in prostate histopathology: where are we in 2021? *Curr Opin Urol*. 2021;31(4):430–435. doi:10.1097/MOU.0000000000000883.
58. Yoshida H, Yamashita Y, Shimazu T, Cosatto E, Kiyuna T, Taniguchi H, et al. Automated histological classification of whole slide images of colorectal biopsy specimens. *Oncotarget*. 2017;8(53):90719–90729. doi:10.18632/oncotarget.21819.
59. Luo H, Xu G, Li C, He L, Luo L, Wang Z, et al. Real-time artificial intelligence for detection of upper gastrointestinal cancer by endoscopy: a multicentre, case-control, diagnostic study. *Lancet Oncol*. 2019;20(12):1645–1654. doi:10.1016/S1470-2045(19)30637-0.
60. Repici A, Badalamenti M, Maselli R, Correale L, Radaelli F, Rondonotti E, et al. Efficacy of Real-Time Computer-Aided Detection of Colorectal Neoplasia in a Randomized Trial. *Gastroenterology*. 2020;159(2):512–520.e7. doi:10.1053/j.gastro.2020.04.062.

61. Carrio A, Sampedro C, Sanchez-Lopez JL, Pimienta M, Campoy P. Automated Low-Cost Smartphone-Based Lateral Flow Saliva Test Reader for Drugs-of-Abuse Detection. *Sensors*. 2015;15(11):29569–29593. <https://doi.org/10.3390/s151129569>.
62. Foysal KH, Seo SE, Kim MJ, Kwon OS, Chong JW. Analyte Quantity Detection from Lateral Flow Assay Using a Smartphone. *Sensors*. 2019;19(21):4812. <https://doi.org/10.3390/s19214812>.
63. Yan W, Wang K, Xu H, Huo X, Jin Q, Cui D. Machine Learning Approach to Enhance the Performance of MNP-Labeled Lateral Flow Immunoassay. *Nano-Micro Letters*. 2019;11. doi:10.1007/s40820-019-0239-3.
64. Tania MH, Lwin KT, Shabut AM, Najlah M, Chin J, Hossain MA. Intelligent image-based colourimetric tests using machine learning framework for lateral flow assays. *Expert Systems with Applications*. 2020;139:112843. <https://doi.org/10.1016/j.eswa.2019.112843>.
65. Ye X, Zheng C, Chen J, Gao Y, Murray CB. Using binary surfactant mixtures to simultaneously improve the dimensional tunability and monodispersity in the seeded growth of gold nanorods. *Nano Lett*. 2013;13(2):765–71. doi:10.1021/nl304478h.
66. Cardarelli M, Mariotti D, Pomponi M, Spanò L, Capone I, Costantino P. *Agrobacterium rhizogenes* TDNA gene capable of inducing hairy root phenotype. *Mol. Gen. Genet*. 1987;209:475–480. <https://doi.org/10.1007/BF00331152>.
67. Schmitz GG, Walter T, Seibl R, Kessler C. Nonradioactive labeling of oligonucleotides in vitro with the hapten digoxigenin by tailing with terminal transferase. *Anal Biochem*. 1991;192(1):222–31. doi:10.1016/0003-2697(91)90212-c.
68. Pedregosa F, Varoquaux G, Gramfort A, Michel V, Thirion B, Grisel O, et al. Scikit-learn: Machine Learning in Python. *Journal of Machine Learning Research* 2011;12(85):2825–2830.
69. Doyle JJ, Doyle JL. A rapid procedure for DNA purification from small quantities of fresh leaf tissue. *Phytochem Bull*. 1987;19:11–15.
70. Clarke JD. Cetyltrimethyl ammonium bromide (CTAB) DNA miniprep for plant DNA isolation. *Cold Spring Harb Protoc*. 2009;2009(3):pdb.prot5177. doi:10.1101/pdb.prot5177.
71. Healey A, Furtado A, Cooper T, Henry RJ. Protocol: a simple method for extracting next-generation sequencing quality genomic DNA from recalcitrant plant species. *Plant Methods*. 2014;10:21. doi:10.1186/1746-4811-10-21.
72. Serwer P. Agarose gels: Properties and use for electrophoresis. *Electrophoresis*. 1983;4(6):375–382. <https://doi.org/10.1002/elps.1150040602>.
73. Zimm BH, Levene SD. Problems and prospects in the theory of gel electrophoresis of DNA. *Quarterly Reviews of Biophysics*. 1992;25(2):171–204. doi:10.1017/s0033583500004662.
74. Lide DR. *CRC Handbook of Chemistry and Physics*. 86th ed. Boca Raton: CRC Press; 2005.
75. Hölteke HJ, Ankenbauer W, Mühlegger K, Rein R, Sagner G, Seibl R, et al. The Digoxigenin (DIG) System for non-radioactive labeling and detection of nucleic acids-an overview. *Cell. Mol. Biol*. 1995;41(7):883–905.
76. Deegan RD, Bakajin O, Dupont TF, Huber G, Nagel SR, Witten TA. Capillary flow as the cause of ring stains from dried liquid drops. *Nature* 1997;389:827–829. <https://doi.org/10.1038/39827>.

Additional file 1

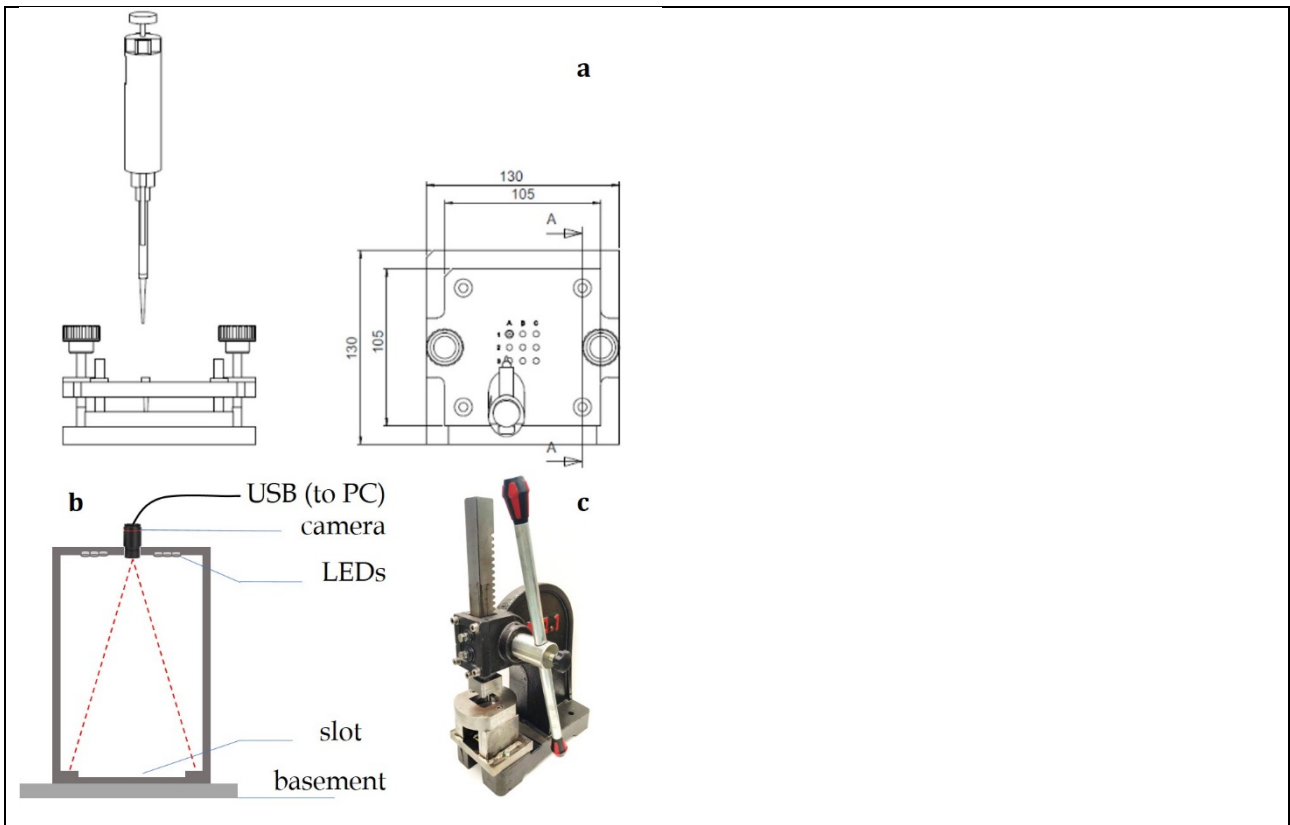


Figure S1: a) technical drawings of the dispenser, b) schematic diagram of the darkroom, and c) photograph of the cutter specifically designed for standardized preparation and imaging of dot-blot membranes.

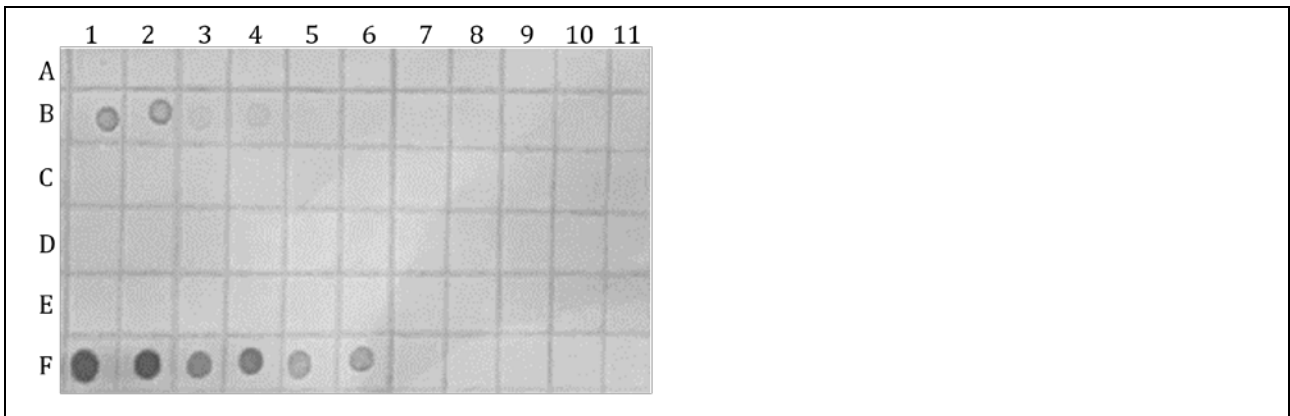


Figure S2: Preliminary dot-blot assay performed by using a DIG-labeled probe. **A:** *rolC* fw primer (negative control); **B:** *rolC* fw primer fully complementary sequence (positive control); **C, D, E:** *rolC* fw primer complementary oligonucleotides with one deletion and none (C), one (D) or two transversions (E). Decreasing concentrations (1, 10^{-1} , 10^{-2} , 10^{-3} , 10^{-4} nM) were immobilized in all lines from A to E, in duplicate. **F:** pUC19::*rolC* vector at 50, 10, 1 ng/μl in duplicate. Column 11 contains aliquots of the same aqueous used to dilute each target.

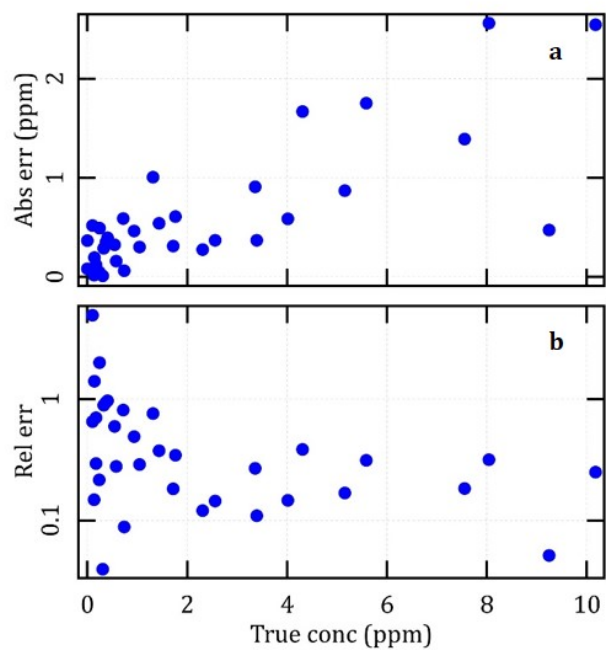


Figure S3: Analysis of the absolute errors of the leave-one-out cross validation predictors presented in Figure 5 and expressed in absolute **(a)** and relative terms **(b)**.

Supplementary Files

This is a list of supplementary files associated with this preprint. Click to download.

- [Centietalgraphicalabstract.jpg](#)